Fast and Reversible Li Ion Insertion in Carbon-Encapsulated Li_3VO_4 as Anode for Lithium-Ion Battery

*Changkun Zhang, Huanqiao Song, Chaofeng Liu, Yaguang Liu, Cuiping Zhang, Xihui Nan, and Guozhong Cao**

Carbon-encapsulated Li_3VO_4 is synthesized by a facile environmentally benign solid-state method with organic metallic precursor $VO(C_5H_7O_2)_2$ being chosen as both V and carbon sources yielding a core–shell nanostructure with lithium introduced in the subsequent annealing process. The Li_3VO_4 encapsulated with carbon presents exceeding rate capability (a reversible capability of 450, 340, 169, and 106 mAh g^{-1} at 0.1 C, 10 C, 50 C, and 80 C, respectively) and long cyclic performance (80% capacity retention after 2000 cycles at 10 C) as an anode in lithium-ion batteries. The superior performance is derived from the structural features of the carbon-encapsulated Li_3VO_4 composite with oxygen vacancies in Li_3VO_4, which increase surface energy and could possibly serve as a nucleation center, thus facilitating phase transitions. The in situ generated carbon shell not only facilitates electron transport, but also suppresses Li_3VO_4 particle growth during the calcination process. The encouraging results demonstrate the significant potential of carbon encapsulated Li_3VO_4 for high power batteries. In addition, the simple generic synthesis method is applicable to the fabrication of a variety of electrode materials for batteries and supercapacitors with unique core–shell structure with mesoporous carbon shell.

1. Introduction

Lithium-ion batteries (LIBs) with high energy density and efficiency have been considered one of the most important electrochemical energy storage systems.[1,2] Extensive research and development on this technology have delivered portable electronics and cars.[3] Generally, there are three main anode materials: one is the alloy-type materials such as Si,[4] Sn,[5] and Ge[6,7] based alloys and their composites,[8] another is the conversion reaction type such as transition metal oxides,[9–11] metal sulfides,[12] and the third is the intercalation type such as graphite, Ti,[13,14] and V-based oxides.[15,16] For 20 years graphite is the main commercial LIBs anode material. Improving on the energy storage of graphite is the task of researchers involved in the development of anode materials.

Dr. C. Zhang, Dr. H. Song, C. Liu, Y. Liu, C. Zhang, X. Nan, Prof. G. Cao
Beijing Institute of Nanoenergy and Nanosystems
Chinese Academy of Sciences
Beijing 100083, China
E-mail: gzcao@u.washington.edu
Prof. G. Cao
Department of Materials Science and Engineering
University of Washington
Seattle 98185-2120, WA, USA

DOI: 10.1002/adfm.201500644

Although, as a zero-strain insertion material, spinel $Li_4Ti_5O_{12}$ possesses good reversibility and excellent Li^+ mobility in the charge–discharge process, it has a low theoretical capacity (175 mAh g^{-1}) and a relatively high potential at ≈1.54 V versus Li^+/Li that limited the energy density of the full cell with the $Li_4Ti_5O_{12}$ anode.[17,18] The classical layered frameworks of vanadium oxides such as V_2O_5,[19] $Li_xV_2O_5$,[20] and LiV_3O_8[21] can host Li^+ intercalation and are usually taken as cathode materials. $Li_{1+x}V_{1-x}O_2$ has a layered structure with a hexagonal system and a theoretical volumetric capacity of 1064 mAh cm^{-3} compared to graphite of 790 mAh cm^{-3}.[22,23] Li^+ ions can be intercalated into the layered structure at low potential (≈0.1 V),[24] which is similar to graphite as an anode; however, the low practical capacity and poor cycling performance limit its application. Recently, Li_3VO_4 (LVO) has been studied as a new insertion anode material for LIBs.[25–28] It composes of corner-shared VO_4 and LiO_4 tetrahedrons (Figure S1, Supporting Information). Li^+ ions are expected to reversibly intercalate into empty sites in the structure. As an intercalation electrode, LVO has small structural and volume changes and fast movement of Li^+ ions.[29] Compared with other intercalation materials, Li^+ ions can be intercalated into the LVO mainly at the voltage range between 0.5 and 1.0 V, and theoretical gravimetric capacity is 394 mAh g^{-1} (1 C ≈ 400 mAh g^{-1}), corresponding to $x = 2$ in $Li_{3+x}VO_4$.[26,27] Combined with the low but safe voltage, large specific capacity, and low cost, LVO has been considered one promising anode material. Meanwhile, despite LVO having high ionic conductivity (≈10^{-4} S m^{-1}),[30] the electrical conductivity is low that causes large resistance polarization in LIBs. Carbon nanotube/LVO[28] and graphene/LVO[27,31] composites have been investigated to enhance electron transport, but the high rate performance is still not attained so far. On the other hand, LVO synthesized by conventional solid-state sintering,[25,26,29,32] sol–gel processing,[31] and hydrothermal growth[33] has large particle size, which leads to low specific surface area and slow Li^+ diffusion process. Therefore, achieving LVO with small particle size for high storage capacity particularly at a high rate remains a great challenging at present.

Herein, we report a novel strategy for the fabrication of nanostructured carbon coated LVO by a one-step solid-state reaction in the absence of external carbon sources. In this

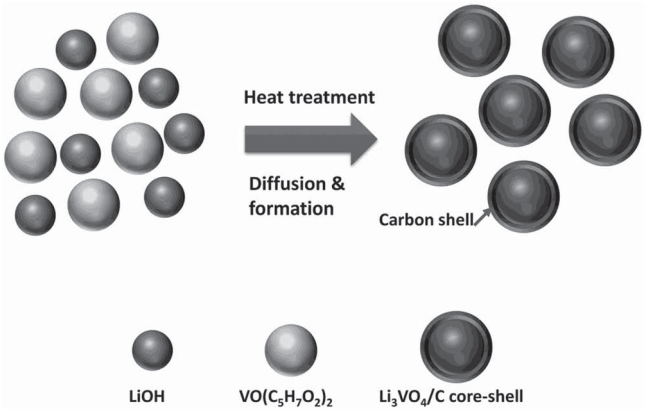

Figure 1. Schematic diagram of the synthesis procedure of the Li_3VO_4/C core–shell composite.

method, the organic metallic precursor $VO(C_5H_7O_2)_2$ was chosen as both V and carbon sources yielding a core–shell morphology. The resulting unique carbon encapsulated LVO (LVO/C) material exhibits superior rate capability (a reversible capability of 340, 256, 169, and 106 mAh g^{-1} at 10 C, 20 C, 50 C, and 80 C, respectively) and excellent cycling stability (80% capacity retention after 2000 cycles at 10 C) for high power LIBs.

2. Results and Discussion

In the solid-state method, $VO(C_5H_7O_2)_2$ is mixed with the lithium salt LiOH, and then calcinated at 600 °C for 2 h in 1 atm argon. **Figure 1** shows the schematic diagram of the synthesis procedure. $VO(C_5H_7O_2)_2$ with low decomposition temperature (≈280 °C) decomposes first to form a vanadium oxide core with carbon shell. With the increase of the annealing temperature, the LiOH diffuses through the carbon layer to react with the vanadium oxide core. The formed carbon shell effectively suppresses particle growth during annealing, resulting in small LVO particle with a uniform carbon shell. The total reaction equation was as follows:

$$VO(C_5H_7O_2)_2 + 3LiOH \xrightarrow{600\ ^\circ C} Li_3VO_4 + 4.5C_2H_2 + C + 4H_2O \quad (1)$$

For comparison, the pristine LVO was prepared by a modified solid-state method as briefly described below. V_2O_5 was first dissolved in a LiOH solution and then, the mixture was sonicated for 10 min and stirred for 10 h. The precursor was collected and treated at 55 °C for 12 h. The dried composite was subsequently treated at 600 °C for 2 h.

Figure 2a presents the XRD patterns of the products. It can be seen that the diffraction peaks of both LVO and LVO/C samples can be indexed into an orthorhombic LVO structure (JCPDS No. 38-1247, Figure S1, Supporting Information). No crystalline peak of carbon was observed in LVO/C. The grain sizes estimated from (111) peak using the Debye–Scherrer equation are 102 and 42 nm for LVO and LVO/C, respectively. Raman spectra shown in Figure 2b confirmed that carbon existed in the LVO/C composite. The peaks at 1335 and 1585 cm^{-1} correspond to the D band (sp^3 hybridization) and G band (sp^2 hybridization) of graphitic carbon, respectively. The peak intensity ratio (I_D/I_G) is usually used to measure the degree of crystallinity of carbon.[34] The I_D/I_G ratio of the LVO/C composite is 1.09, indicating an enhancement of the degree of graphitization.

The X-ray photoelectron spectra (XPS) of LVO and LVO/C are shown in **Figure 3**. The peak at 517.3 eV corresponds to the binding energy of the $V2p_{3/2}$ electrons for vanadium in the pentovalent state. The peak at 515.8 eV is due to the partial reduction of the pentovalent ions to tetravalent ions during the annealing Ar atmosphere. The molar ratio of the V^{4+} to V^{5+} ions in LVO was 0.07 (Figure 3a) and 0.08 for LVO/C (Figure 3). The presence of V^{4+} in the LVO sample can be attributed to the inert annealing atmosphere. A little more V^{4+} in the LVO/C sample may stem from the generated carbon reduction. The presence of surface defects such as oxygen vacancies increases surface energy and could possibly serve as a nucleation center, thus facilitating phase transitions.[35] The electrical conductivity of the LVO/C composite measured by the four-point probe system is 0.54 S cm^{-1}, improved by nearly five orders of magnitude (≈5.8×10^{-6} S cm^{-1} for LVO.[36] Such a drastic enhancement in electrical conductivity is attributed to the well-connected

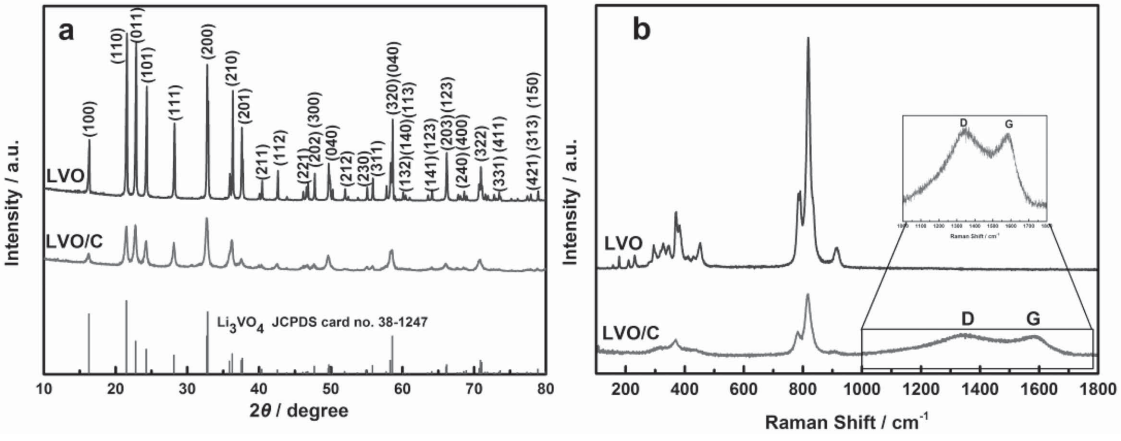

Figure 2. a) XRD patterns and b) Raman spectra of the LVO and the LVO/C composite.

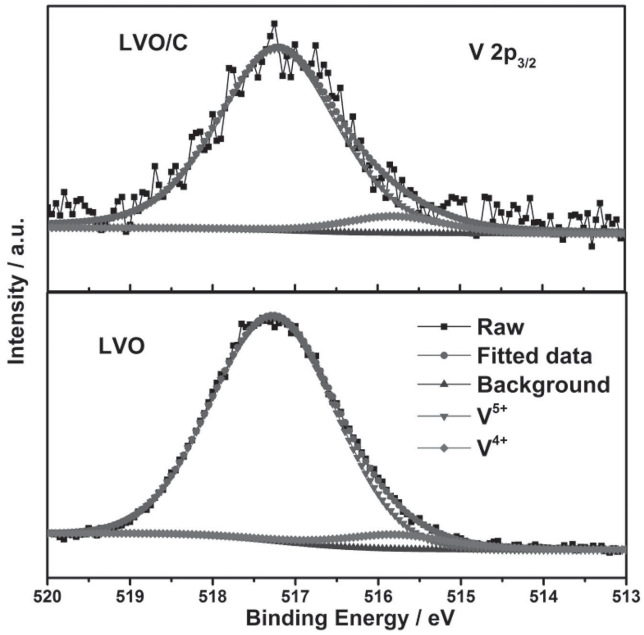

Figure 3. X-ray photoelectron spectroscopy (XPS) spectra for $V2p_{3/2}$ of LVO and LVO/C composites.

carbon, although the presence of tetravalent vanadium ions and oxygen vacancies may also improve the electrical conductivity, albeit small comparing with the contribution of carbon.

The morphology and microstructure of the LVO/C composite were characterized using a field emission scanning electron microscopy (SEM) and a transmission electron microscope (TEM). The SEM and TEM images in **Figure 4**a,b reveal that the synthesized LVO/C composite is of 20–75 nm in size, while the particle size of the LVO prepared by sintering of V_2O_5 and LiOH mixture (Figure S2, Supporting Information) is about 0.8–2.0 μm. The resulted carbon decomposed from $VO(C_5H_7O_2)_2$ has the advantage of preventing particle growth during annealing. Figure 4c,d reveals that a thin carbon shell (2–5 nm in thickness) has coated onto LVO to form an LVO/C core–shell nanostructure. The high-resolution (HR) TEM image in Figure 4d shows clear lattice fringes with an interfringe spacing of 0.41 nm, corresponding to the *d*-spacing of (110) planes of LVO.

Nitrogen sorption isotherms were generated to investigate the Brunauer–Emmet–Teller (BET) surface area and the porous structure of the LVO/C. The nitrogen adsorption–desorption isotherm of the LVO/C composite (**Figure 5**a) exhibits a typical III isotherm with a distinct hysteresis loop that is consistent with the presence of the distinct porous structure. The BET surface area and pore volume of LVO/C composite are 64 $m^2\ g^{-1}$ and 0.119 $cm^3\ g^{-1}$, respectively. The pore size distribution (Figure 5a, inset) according to the Barrett–Joyner–Halenda (BJH) method indicates that the LVO/C is a mesoporous composite with a relatively broad pore size distribution of 2–32 nm and the average pore size of 9.0 nm. The amount of carbon in the LVO/C composite was estimated to be approximately 9.2 wt% from the thermogravimetric analysis (TGA, Figure 5b), which is much lower than the calculated result (Figure S3, Supporting Information). It can be inferred that the carbon shell is a mesoporous structure combined with the pore size distribution. Li^+ ions can easily pass through the porous carbon shell for the insertion/extraction reaction with LVO. Moreover, LVO crystallites are connected to each other through the carbon, thereby ensuring electrical continuity around the crystallites.

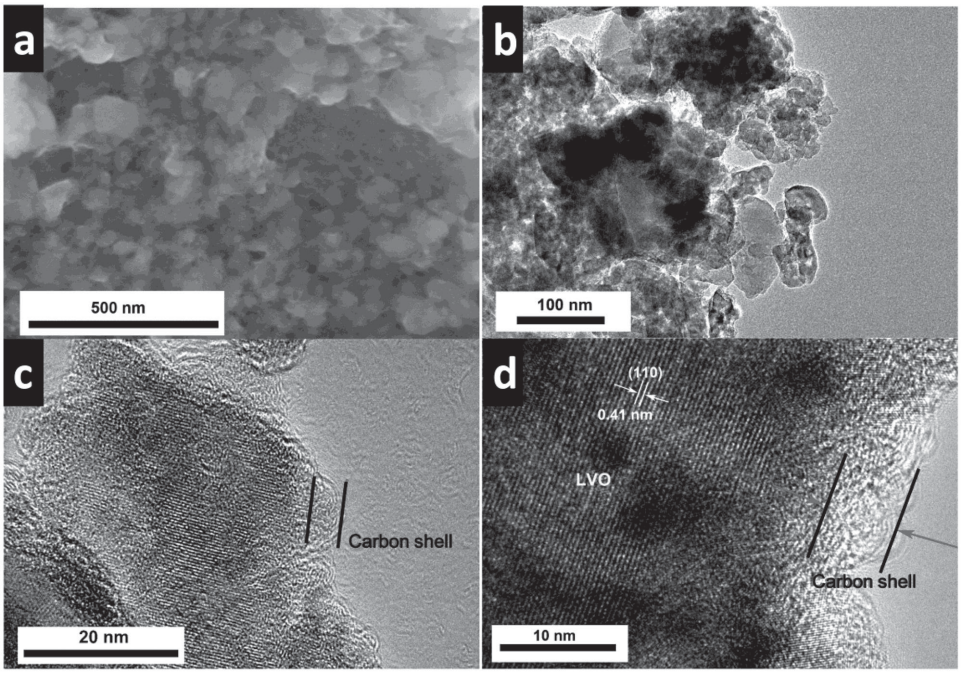

Figure 4. a) SEM and b–d) TEM images of the LVO/C core–shell composite synthesized by $VO(C_5H_7O_2)_2$ and LiOH at 600 °C for 2 h under Ar atmosphere.

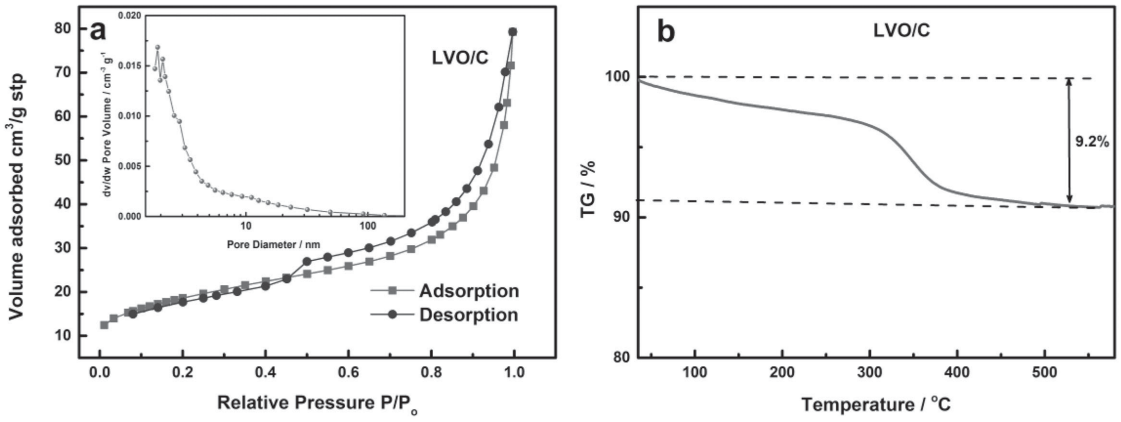

Figure 5. a) The N_2 adsorption–desorption isotherm of the as-prepared LVO/C. Inset: the pore size distribution; b) thermogravimetric curve of the LVO/C core–shell structure at 10 °C min^{-1} in air.

The electrochemical performance of the as-synthesized materials was analyzed in CR2032 coin cells. In order to compare the performance with the literature, the electrode was made by 75% of active materials, 20% of acetylene black, and 5% of sodium carboxymethyl cellulose (CMC) in weight.[25,27,28] The loading of the active materials was 0.8–1.1 mg cm^{-2}. The bare LVO showed the first discharge capacity of only 397 mAh g^{-1} at 0.1 C (Figure S4, Supporting Information), while the LVO/C electrode delivered a discharge capacity of 569 mAh g^{-1} at the first cycle (**Figure 6**a). The intercalation of Li^+ occurs at a voltage range below 1.0 V and above 0.5 V versus Li/Li^+. The second discharge capacity of LVO/C electrode is 450 mAh g^{-1} that is lower than the initial discharge, resulting from the formation of the solid electrolyte interface (SEI) film. The Coulombic efficiency is nearly 100% after the first cycle. At 0.1 C, the capacity of the LVO/C electrode is higher than the theoretical value because of the acetylene black's contribution. To explore the capacity contribution of the acetylene black in the electrode, the rate performance of the acetylene black was measured at the same current densities, ranging from 0.1 to 80 C (Figure S5a, Supporting Information). The capacity of the acetylene black anode is 217 mAh g^{-1} at 0.1 C. The actual capacity of the LVO/C can be calculated to be 392 mAh g^{-1} (very close to its theoretical capacity) at 0.1 C. Details of the capacity contribution ratio of the acetylene black in the electrode the are shown in Figure S5b (Supporting Information).

The rate performance was investigated at different cycling rates. In Figure 6c, it can be seen that the LVO/C electrode exhibits higher capacity than the pristine LVO. The discharge capacities of LVO/C electrode are observed at about 410, 395, 368, 340, 256, and 169 mAh g^{-1} at rates of 1 C, 2 C, 5 C, 10 C, 20 C, and 50 C, respectively. Even when increasing the cycling rate up to 80 C (32 A g^{-1}), the discharge capacity can be retained at 106 mAh g^{-1}, whereas the capacity of LVO is almost zero.

To further confirm the enhanced cycling stability, both of the LVO/C and LVO electrodes exhibit stable cycling performance after 50 cycles at 0.1 C (Figure 6c). The discharge capacity of the LVO/C electrode is 401 mAh g^{-1} after 50 cycles, which is higher than this of LVO, and the Coulombic efficiency remained constant at approximately 100%. Furthermore, as shown in Figure 6d, the capacity of the LVO/C electrode can be maintained 80% retention of the initial reversible capacity after 2000 cycles at the high 10 C (4 A g^{-1}). The durability for LVO/C is superior to the reported vanadium-based anode materials.[25,27,28,31] The good retention of capacity can also be proved by the SEM images after cycling (Figure S6, Supporting Information).

Cyclic voltammetry (CV) of the LVO/C electrode was also performed at a scan rate of 0.2 mV s^{-1} versus Li/Li^+ between 0.2 and 3.0 V, as shown in **Figure 7**a. For the first cycle, two peaks at 0.54 and 0.73 V can be attributed to the phase transformation with the insertion of Li^+ ions into LVO. The two reduction peaks are shifted to 0.83 and 0.52 V in the second cycles. Only one oxidation peak in the first anodic scan is corresponding to the Li^+ ion extraction from $Li_{3+x}VO_4$. Another weak oxidation peak is found in the following cycling at 0.76 V, which can be observed clearly at a higher scan rate (Figure 7b). The intercalation and deintercalation reactions during the charge and discharge processes can be shown as Equation (2)

$$Li_3VO_4 + xLi^+ + xe^- \Leftrightarrow Li_{3+x}VO_4 \quad (0 \le x \le 2) \tag{2}$$

CV curves of the LVO/C electrode are also measured at the different scan rates from 0.2 to 1.2 mV s^{-1} (Figure 7b). The reduction peak shifts to a low potential region along with the increasing of scan rate, whereas the oxidation peaks shift to a high potential region. Based on the Randles–Sevchik equation for semi-infinite diffusion of Li^+ ions into LVO, the apparent diffusion coefficients were calculated as Equation (3)[37]

$$I_p = 0.4463\left(\frac{F^3}{RT}\right)^{1/2} n^{3/2} A D^{1/2} C_0 v^{1/2} \tag{3}$$

where I_p is the peak current, R is the gas constant, T is the absolute temperature, F is the Faraday constant, n is the number of electrons transferred per molecule, A is the active surface area of the electrode (0.50 cm^2), C_0 is the concentration of Li^+ ions in the cathode (9.8×10^{-3} mol cm^{-3}), D is the apparent ion diffusion coefficient, and v is the scanning rate. From the slope of the fitting line collected from oxidation peak current (I_{pa}) (Figure 7c), the apparent diffusion coefficient D of LVO/C is 4.13×10^{-11} cm^2 s^{-1},

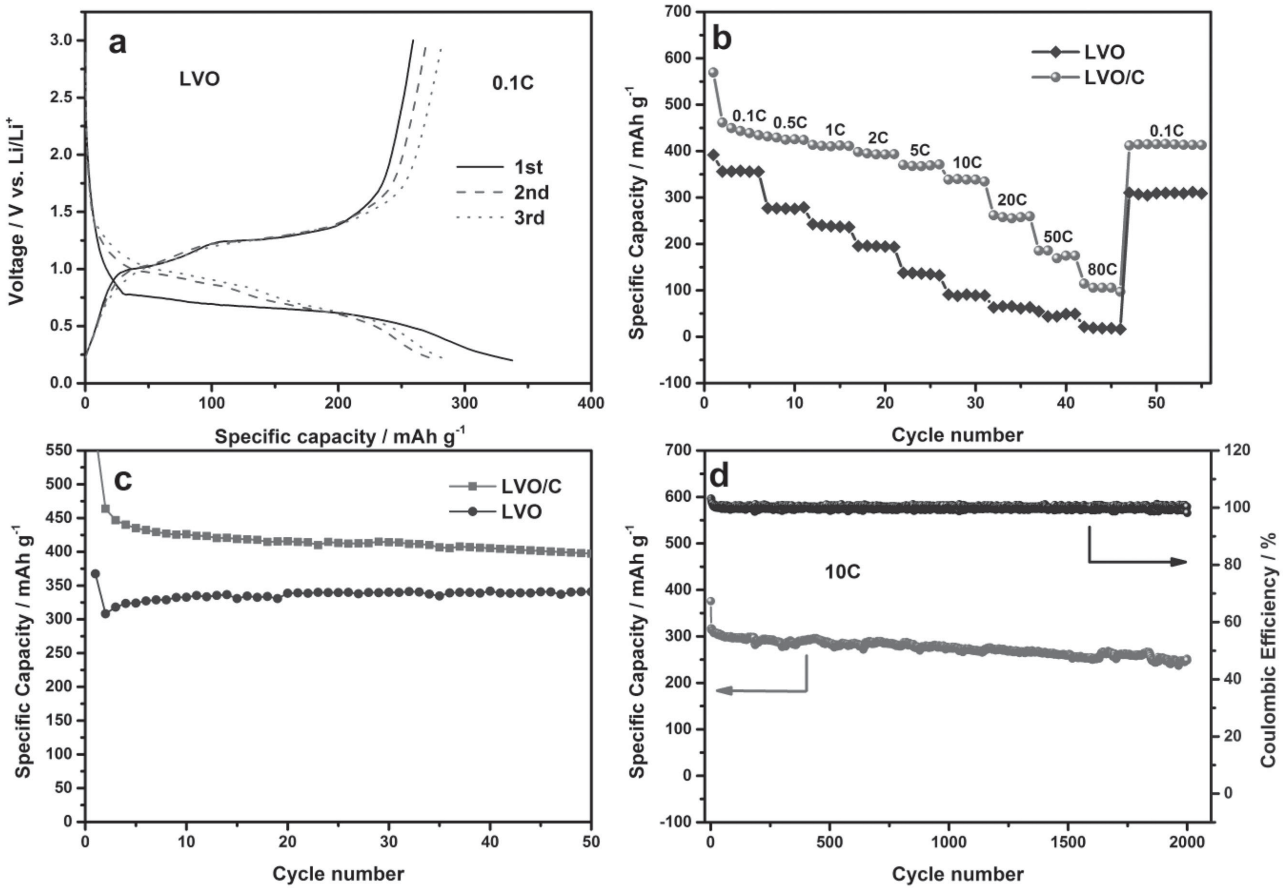

Figure 6. a) Galvanostatic discharge and charge profiles of the LVO/C composite in the voltage range of 0.2–3 V versus Li/Li^+ at a rate of 0.1 C; b) discharge capacities of LVO and the LVO/C composite at different rates between the voltage range of 0.2 and 3 V versus Li/Li^+; c) cycling performance at 0.1 C between 0.2 and 3 V versus Li/Li^+; d) long-term cycling performance of the LVO/C composite at 10 C between 0.2 and 3 V versus Li/Li^+(4 A g^{-1}). All capacity calculations are based on the mass of LVO/C.

higher than those of LVO (3.4×10^{-11} cm^2 s^{-1}, calculated in Figure S7 in the Supporting Information).

The electrochemical impedance spectrum (EIS) of the electrodes after three cycles has been provided in Figure 7d. The EIS spectrum shows the compressed semicircle from the high to medium frequency range of each spectrum, which describes the charge transfer resistance (R_{ct}) and constant-phase element (CPE, representing the double-layer capacitance, taking into account the roughness of the particle surface) for these electrodes, and a line inclined at approximately 45° at the low frequency, corresponding to the Warburg impedance (W) that is related to the Li^+ ions diffusion within the particles. After simulating the second compressed semicircle for both samples, the values of R_{ct} for the LVO and the hollow LVO/C electrodes were calculated to be 180.2 and 38.7 Ω, respectively, suggesting that the LVO/C core–shell composite has faster kinetics for Li^+ ion insertion/extraction. Another semicircle was detected in the low-frequency range of 100–0.1 Hz when the cell voltage was below 1.55 V (Figure S8, Supporting Information). It is attributed to the bulk resistance (R_b) arising from changing of LVO crystalline structure after lithiation. It has been confirmed that the higher activation energy for Li mobility under lithiated state limits Li^+ ion transport in bulk.[38–40] Meanwhile, the reversible semiconductor–metal transformations during the charge–discharge process also lead to large changes in R_b values for some other materials.[41–43]

Figure 8 shows a comparison of performance of the LVO/carbon materials from this study and reported in open literature. The LVO/C composite in this work not only exhibits superior reversible capacity than the reported other LVO/carbon materials, but also shows a longer cycling performance at a high rate.[27,28,31] Although the exact mechanism for such an improvement in electrochemical properties is complex and needs a further study, the high rate performance and durability of LVO/C composite could be attributed to the following advantages of unique nano core–shell structure with oxygen vacancies. First, the carbon-encapsulated LVO with small particle size and porous carbon shell provides high specific surface area and fast Li^+ transport. Second, the in situ generated mesoporous carbon shell has more contact between carbon and LVO than the ex situ coated graphene and carbon nanotube, which favors the relaxation of the strain/stress and the retention of good structural stability during cycling.[27] Third, in addition to facilitating the electron transport, the carbon also induced more tetravalent vanadium ions and oxygen vacancies during the preparation, which may benefit the electronic conduction.[44]

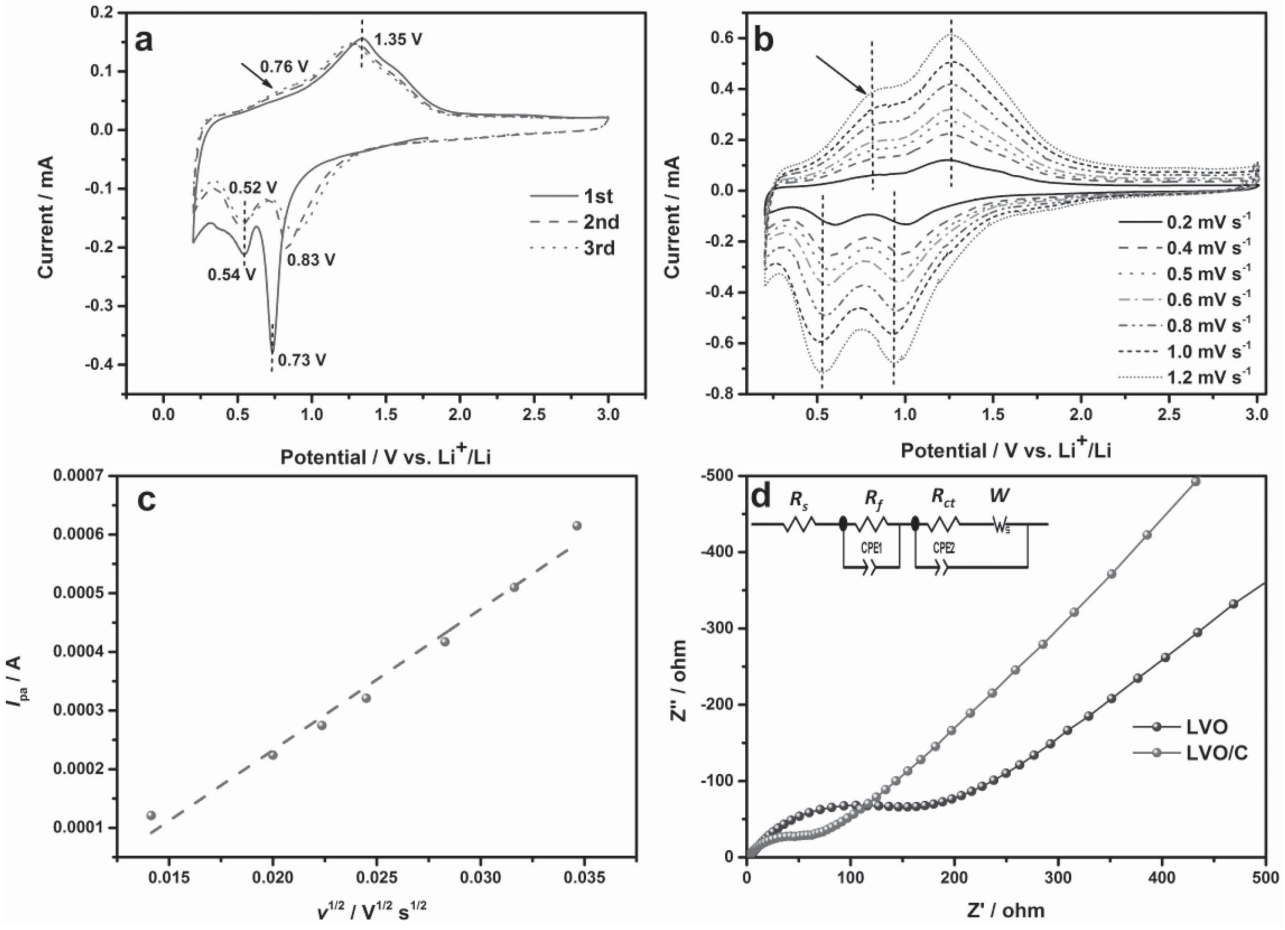

Figure 7. a) Cyclic voltammetry curve of the LVO/C composite at a scan rate of 0.2 mV s^{-1}; b) cyclic voltammetry curves of the LVO/C electrode at a different scan rate; c) dependence of oxidation peak current (I_{pa}) on the square rate of scan rate for LVO/C electrode; d) Nyquist plots for the LVO and LVO/C electrodes after three cycles (the AC amplitude was 5 mV, and the frequency range applied was 0.1 Hz to 100 kHz at an anodic potential of 2.4 V vs Li^+/Li). Inset: the equivalent circuit used to describe the charge process.

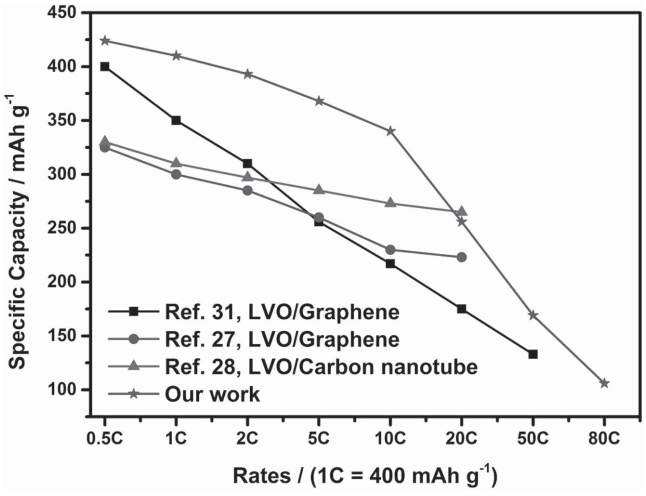

Figure 8. Electrochemical performance of the LVO/carbon anode material compared with other previous works.

The presence of both tetravalent vanadium ions and oxygen vacancies on the surface of LVO/C may have appreciably promoted the electrochemical reactions at the interface between the electrode and electrolyte as demonstrated in V_2O_5 films[35] and TiO_2 nanotube arrays.[45]

3. Conclusion

The carbon encapsulated with LVO material has been synthesized by a simple solid-state process. In this method, the in-situ generated carbon directly and uniform coated on the LVO without the addition of an external carbon source. Meanwhile, the formed mesoporous carbon shell could suppress particle growth during the annealing process. The LVO/C core–shell nanostructure permits fast Li^+ ions and electron transports, enabling superior performance. The resulting LVO/C composite presents excellent high-rate performance with capacities of 450 mAh g^{-1} at 0.1 C, 350 mAh g^{-1} at 10 C, and 106 mAh g^{-1}

even at 80 C (32 A g^{-1}). After 2000 cycles at 10 C, its capacity is maintained 80% retention of the original reversible capacity. These excellent properties make the carbon-encapsulated LVO composite a promising anode candidate for the development of high-performance, low-cost, and advanced LIBs.

4. Experimental Section

Sample Preparation: All reagents in this experiment were used without any further purification. The LVO/C core–shell nanostructured material was synthesized via a simple solid-state reaction. $VO(C_5H_7O_2)_2$ (Sigma-Aldrich, >99%) was mixed with LiOH (Sinopharm Chemical Reagent, >98.0%) and then heated to 600 °C for 2 h at a rate of 10 °C min^{-1} under Ar (>99.999%). The molar ratio of the LiOH to $VO(C_5H_7O_2)_2$ was 3. For comparison, the pristine LVO was prepared by a modified solid-state method. First, V_2O_5 (TianJin··FUChemical, >99.0%) was dissolved in a LiOH solution in deionized water and ethanol. Then, the mixture was sonicated for 10 min and stirred for 10 h. The precursor was collected and treated at 55 °C for 12 h. The dried composite was subsequently treated at 600 °C for 2 h under Ar.

Material Characterization: The crystallographic information of the samples was examined by X-ray diffraction (XRD) on a Marcogroup diffractometer (MXP21 VAHF) with Cu Kα radiation (λ = 1.5418 Å). The morphology and microstructure of the products were characterized by the field-emission scanning electron microscopy (FESEM) and high-resolution transmission electron microscopy (HRTEM, JEOL JEM-2010) measurements. The surface area of LVO/C was determined using nitrogen sorption analyses via Micromeritics surface area and porosity analyzer (ASAP 2020 HD88, USA). The electrical condutivity of LVO/C was measured by a four-point probe testing system (Suzhou Jingge ST2722 Electronic Co., China). X-ray photoelectron spectroscopy (XPS, Thermo Scientific ESCALab 250 Xi spectrometer) with Al KR radiation in twin anode. For the XPS spectra, the binding energy was calibrated using the C 1s photoelectron peak at 284.6 eV as the reference. Thermogravimetry/differential scanning calorimetry (TG/DSC) was performed on a Simultaneous Thermal Analyzer (STA 449F3, NETZSCH, Germany) from 20 to 600 °C in air at a heating rate of 10 °C min^{-1}. Raman spectra were obtained on a MicroRaman Spectrophotometer.

Electrochemical Measurements: The electrochemical performance of the samples was measured using R2032 coin-type cells. Cells were assembled in a glovebox filled with ultrahigh purity argon with water and oxygen contents below 0.1 ppm using NKK TF4840 as the separator and 1 M solution of $LiPF_6$ in ethylene carbonate (EC)/dimethyl carbonate (DMC) (EC/DMC = 1:1 in volume) as the electrolyte. Li foils were used as the counter and reference electrode. The electrode was made by 75% of active material, 20% of acetylene black, and 5% of sodium carboxymethyl cellulose (CMC) in weight. A Cu grid was used as the current collector. The cells were characterized by cyclic voltammetry (CV) and electrochemical impedance spectroscopy (EIS) on a Solartron Instrument, while the galvanostatic discharging/charging measurements were conducted on a LAND (Wuhan, China) automatic battery tester. All the measurements were carried out over the voltage region from 0.2 V to 3.0 V versus Li/Li^+, and the frequency of EIS measurement ranged from 100 kHz to 0.1 Hz. The specific capacity was calculated based on the weight of the active composite material.

Supporting Information

Supporting Information is available from the Wiley Online Library or from the author.

Acknowledgements

This work was supported by the "thousands talents" program for pioneer researcher and his innovation team, China. This work was also supported by the National Science Foundation of China (51374029), Program for New Century Excellent Talents in University (NCET-13-0668), Fundamental Research Funds for the Central Universities (FRF-TP-14-008C1), and China Postdoctoral Science Foundation (2014M550675).

Received: February 15, 2015
Revised: April 2, 2015
Published online: May 4, 2015

[1] D. Larcher, J. M. Tarascon, *Nat. Chem.* **2015**, *7*, 19.
[2] K.-X. Wang, X.-H. Li, J.-S. Chen, *Adv. Mater.* **2015**, *27*, 527.
[3] H. D. Yoo, E. Markevich, G. Salitra, D. Sharon, D. Aurbach, *Mater. Today* **2014**, *17*, 110.
[4] N. Liu, Z. Lu, J. Zhao, M. T. McDowell, H.-W. Lee, W. Zhao, Y. Cui, *Nat. Nano* **2014**, *9*, 187.
[5] Y. Xu, Q. Liu, Y. Zhu, Y. Liu, A. Langrock, M. R. Zachariah, C. Wang, *Nano Lett.* **2013**, *13*, 470.
[6] D. Li, C. Feng, H. K. Liu, Z. Guo, *J. Mater. Chem. A* **2015**, *3*, 978.
[7] J. Liu, K. Song, C. Zhu, C.-C. Chen, P. A. van Aken, J. Maier, Y. Yu, *ACS Nano* **2014**, *8*, 7051.
[8] M. N. Obrovac, V. L. Chevrier, *Chem. Rev.* **2014**, *114*, 11444.
[9] Z. Cai, L. Xu, M. Yan, C. Han, L. He, K. M. Hercule, C. Niu, Z. Yuan, W. Xu, L. Qu, K. Zhao, L. Mai, *Nano Lett.* **2014**, *15*, 738.
[10] J. Lin, Z. Peng, C. Xiang, G. Ruan, Z. Yan, D. Natelson, J. M. Tour, *ACS Nano* **2013**, *7*, 6001.
[11] C. He, S. Wu, N. Zhao, C. Shi, E. Liu, J. Li, *ACS Nano* **2013**, *7*, 4459.
[12] D. Kong, H. He, Q. Song, B. Wang, W. Lv, Q.-H. Yang, L. Zhi, *Energy Environ. Sci.* **2014**, *7*, 3320.
[13] L. Shen, E. Uchaker, X. Zhang, G. Cao, *Adv. Mater.* **2012**, *24*, 6502.
[14] S.-L. Chou, J.-Z. Wang, H.-K. Liu, S.-X. Dou, *J. Phys. Chem. C* **2011**, *115*, 16220.
[15] Y. Li, J. Yao, E. Uchaker, J. Yang, Y. Huang, M. Zhang, G. Cao, *Adv. Energy Mater.* **2013**, *3*, 1171.
[16] D. McNulty, D. N. Buckley, C. O'Dwyer, *J. Power Sources* **2014**, *267*, 831.
[17] G.-N. Zhu, H.-J. Liu, J.-H. Zhuang, C.-X. Wang, Y.-G. Wang, Y.-Y. Xia, *Energy Environ. Sci.* **2011**, *4*, 4016.
[18] Y. Sha, B. Zhao, R. Ran, R. Cai, Z. Shao, *J. Mater. Chem. A* **2013**, *1*, 13233.
[19] A. Q. Pan, H. B. Wu, L. Zhang, X. W. Lou, *Energy Environ. Sci.* **2013**, *6*, 1476.
[20] C. Delmas, S. Brethes, M. Menetrier, *J. Power Sources* **1991**, *34*, 113.
[21] R. Mo, Y. Du, N. Zhang, D. Rooney, K. Sun, *Chem. Commun.* **2013**, *49*, 9143.
[22] A. R. Armstrong, C. Lyness, P. M. Panchmatia, M. S. Islam, P. G. Bruce, *Nat. Mater.* **2011**, *10*, 223.
[23] J. H. Song, H. J. Park, K. J. Kim, Y. N. Jo, J.-S. Kim, Y. U. Jeong, Y. J. Kim, *J. Power Sources* **2010**, *195*, 6157.
[24] N.-S. Choi, J.-S. Kim, R.-Z. Yin, S.-S. Kim, *Mater. Chem. Phys.* **2009**, *116*, 603.
[25] H. Li, X. Liu, T. Zhai, D. Li, H. Zhou, *Adv. Energy Mater.* **2013**, *3*, 428.
[26] S. Ni, X. Lv, J. Ma, X. Yang, L. Zhang, *J. Power Sources* **2014**, *248*, 122.
[27] Y. Shi, J.-Z. Wang, S.-L. Chou, D. Wexler, H.-J. Li, K. Ozawa, H.-K. Liu, Y.-P. Wu, *Nano Lett.* **2013**, *13*, 4715.
[28] Q. Li, J. Sheng, Q. Wei, Q. An, X. Wei, P. Zhang, L. Mai, *Nanoscale* **2014**, *6*, 11072.
[29] W.-T. Kim, Y. U. Jeong, Y. J. Lee, Y. J. Kim, J. H. Song, *J. Power Sources* **2013**, *244*, 557.
[30] Q. Fu, F. Du, X. Bian, Y. Wang, X. Yan, Y. Zhang, K. Zhu, G. Chen, C. Wang, Y. Wei, *J. Mater. Chem. A* **2014**, *2*, 7555.

[31] Z. Jian, M. Zheng, Y. Liang, X. Zhang, S. Gheytani, Y. Lan, Y. Shi, Y. Yao, *Chem. Commun.* **2015**, *51*, 229.
[32] W.-T. Kim, B.-K. Min, H. C. Choi, Y. J. Lee, Y. U. Jeong, *J. Electrochem. Soc.* **2014**, *161*, A1302.
[33] Y. Shi, J. Gao, H. D. Abruna, H.-J. Li, H.-K. Liu, D. Wexler, J.-Z. Wang, Y. Wu, *Chem. A Eur. J.* **2014**, *20*, 5608.
[34] X. Wang, Y. Zhang, C. Zhi, X. Wang, D. Tang, Y. Xu, Q. Weng, X. Jiang, M. Mitome, D. Golberg, Y. Bando, *Nat. Commun.* **2013**, *4*, 2905.
[35] D. Liu, Y. Liu, A. Pan, K. P. Nagle, G. T. Seidler, Y.-H. Jeong, G. Cao, *J. Phys. Chem. C* **2011**, *115*, 4959.
[36] V. Massarotti, D. Capsoni, M. Bini, P. Mustarelli, G. Chiodelli, C. B. Azzoni, P. Galinetto, M. C. Mozzati, *J. Phys. Chem. B* **2005**, *109*, 14845.
[37] A. J. Bard, L. R. Faulkner, *Electrochemical Methods: Fundamentals and Applications* Wiley, New York **1980**, p. 213.
[38] K. Kang, Y. S. Meng, J. Bréger, C. P. Grey, G. Ceder, *Science* **2006**, *311*, 977.
[39] M. S. Islam, C. A. J. Fisher, *Chem. Soc. Rev.* **2014**, *43*, 185.
[40] A. Van der Ven, G. Ceder, *J. Power Sources* **2001**, *97–98*, 529.
[41] F. Nobili, F. Croce, B. Scrosati, R. Marassi, *Chem. Mater.* **2001**, *13*, 1642.
[42] M. Menetrier, I. Saadoune, S. Levasseur, C. Delmas, *J. Mater. Chem.* **1999**, *9*, 1135.
[43] M. V. Reddy, S. Madhavi, G. V. Subba Rao, B. V. R. Chowdari, *J. Power Sources* **2006**, *162*, 1312.
[44] X. Chen, L. Liu, P. Y. Yu, S. S. Mao, *Science* **2011**, *331*, 746.
[45] D. Liu, Y. Liu, B. B. Garcia, Q. Zhang, A. Pan, Y.-H. Jeong, G. Cao, *J. Mater. Chem.* **2009**, *19*, 8789.